

Turbulent drag reduction by sector-shaped counter-flow dielectric barrier discharge plasma actuator

Borui Zheng(郑博睿), Shaojie Qi(齐少杰), Minghao Yu(喻明浩), Jianbo Zhang(张剑波), Linwu Wang(王林武), and Dongliang Bian(卞栋梁)

Citation: Chin. Phys. B, 2025, 34 (**2**): 025205. DOI: 10.1088/1674-1056/ada1c6
Journal homepage: http://cpb.iphy.ac.cn; http://iopscience.iop.org/cpb

What follows is a list of articles you may be interested in

Flow control performance evaluation of a tri-electrode sliding discharge plasma actuator

Borui Zheng(郑博睿), Yuanpeng Liu(刘园鹏), Minghao Yu(喻明浩), Yuanzhong Jin(金元中),Qian Zhang(张倩), and Quanlong Chen(陈全龙)
Chin. Phys. B, 2023, 32 (**9**): 095203. DOI: 10.1088/1674-1056/acae76

Post-solitons and electron vortices generated by femtosecond intense laser interacting with uniform near-critical-density plasmas

Dong-Ning Yue(岳东宁), Min Chen(陈民), Yao Zhao(赵耀), Pan-Fei Geng(耿盼飞), Xiao-Hui Yuan(远晓辉), Quan-Li Dong(董全力), Zheng-Ming Sheng(盛政明), and Jie Zhang(张杰)
Chin. Phys. B, 2022, 31 (**4**): 045205. DOI: 10.1088/1674-1056/ac46c5

UAV flight test of plasma slats and ailerons with microsecond dielectric barrier discharge

Zhi Su(苏志), Jun Li(李军), Hua Liang(梁华), Bo-Rui Zheng(郑博睿), Biao Wei(魏彪), Jie Chen(陈杰), Li-Ke Xie(谢理科)
Chin. Phys. B, 2018, 27 (**10**): 105205. DOI: 10.1088/1674-1056/27/10/105205

Modeling and optimization of the multichannel spark discharge

Zhi-Bo Zhang(张志波), Yun Wu(吴云), Min Jia(贾敏), Hui-Min Song(宋慧敏), Zheng-Zhong Sun(孙正中), Ying-Hong Li(李应红)
Chin. Phys. B, 2017, 26 (**6**): 065204. DOI: 10.1088/1674-1056/26/6/065204

Electric and plasma characteristics of RF discharge plasma actuation under varying pressures

Huimin Song(宋慧敏), Min Jia(贾敏), Di Jin(金迪), Wei Cui(崔巍), Yun Wu(吴云)
Chin. Phys. B, 2016, 25 (**3**): 035204. DOI: 10.1088/1674-1056/25/3/035204

Turbulent drag reduction by sector-shaped counter-flow dielectric barrier discharge plasma actuator

Borui Zheng(郑博睿)[1,4,5], Shaojie Qi(齐少杰)[2,4], Minghao Yu(喻明浩)[2,†], Jianbo Zhang(张剑波)[1,4,5], Linwu Wang(王林武)[1,4,5], and Dongliang Bian(卞栋梁)[3]

[1] *School of Automation and Information Engineering, Xi'an University of Technology, Xi'an* 710048, *China*
[2] *School of Mechanical and Precision Instrument Engineering, Xi'an University of Technology, Xi'an* 710048, *China*
[3] *Science and Technology on Plasma Dynamics Laboratory, Air Force Engineering University, Xi'an* 710038, *China*
[4] *Shaanxi Key Laboratory of Complex System Control and Intelligent Information Processing, Xi'an* 710048, *China*
[5] *Shaanxi University Key Laboratory of Photonic Power Devices and Discharge Regulation, Xi'an* 710048, *China*

(Received 3 September 2024; revised manuscript received 30 November 2024; accepted manuscript online 20 December 2024)

The primary objective in aircraft transportation is to minimize turbulent drag, thereby conserving energy and reducing emissions. We propose a sector-shaped counter-flow dielectric barrier discharge plasma actuator, which leverages jet synthesis for drag reduction. A drag control experiment was conducted in a low-speed wind tunnel with a controlled flow velocity of 9.6 m/s ($Re = 1.445 \times 10^4$). This study investigated the effects of varying pulse frequencies and actuation voltages on the turbulent boundary layer. Using a hot-wire measurement system, we analyzed the pulsating and time-averaged velocity distributions within the boundary layer to evaluate the streamwise turbulent drag reduction. The results show that the local TDR decreases as the pulse frequency increases, reaching a maximum reduction of approximately 20.97% at a pulse frequency of 50 Hz. In addition, as the actuation voltage increases, the friction coefficient decreases, increasing the drag reduction rate. The maximum drag reduction of approximately 33.34% is achieved at an actuation voltage of 10 kV.

Keywords: plasma flow control, turbulent boundary layer, turbulent drag reduction

PACS: 52.25.Gj, 52.30.–q, 52.35.Ra, 52.35.We

DOI: 10.1088/1674-1056/ada1c6 **CSTR:** 32038.14.CPB.ada1c6

1. Introduction

With global efforts towards carbon peaking and carbon neutrality, countries are seeking ways to decrease carbon emissions and enhance energy utilization. In civil aviation, reducing flight drag is crucial for improving fuel efficiency. Turbulent frictional drag constitutes a significant portion, comprising more than one-third of the total flight drag.[1] Hence, reducing turbulent frictional drag can yield up to a 10% reduction in total flight drag, thereby enhancing fuel efficiency and potentially saving approximately $3 billions.[2,3] In addition, decreasing turbulent frictional drag can improve the maneuverability and endurance of large military transport aircraft and high-altitude, long-endurance unmanned aerial vehicles (UAVs).

Both passive and active control methods are available for turbulent drag reduction (TDR).[4,5] Passive TDR techniques, including vortex generators,[6] Gurney flaps[7] and grooves,[8] utilize simple and fixed equipment and are typically limited to specific scenarios. Conversely, active TDR techniques, such as wall blowing/suction,[9] synthetic jets[10,11] and DBD plasma actuators,[12] introduce energy into the flow field, allowing for dynamic flow control through adjustable actuation parameters.

The main objective of controlling the turbulent boundary layer (TBL) is to regulate its coherent structures. Dielectric barrier discharge (DBD) control is an active flow control method utilizing plasma pneumatic actuation. Various plasma actuators and numerous different actuation methods have been proposed as innovative approaches to achieve flow-field control.[13–16] Choi's research team explored the influence of spanwise oscillation on the plasma generated above the DBD plasma actuator.[17–19] This method primarily disrupts the near-wall coherent structures of the TBL and has proved to be highly effective. These studies have demonstrated the flow control performance of the DBD actuator. However, the output momentum generated by conventional DBD actuators is relatively weak.

By adding a third electrode to the traditional DBD actuator, Liu was able to improve jet direction control, which can be regulated by connection to a DC power source. With increased actuation intensity, Liu achieved control over different discharge modes in a wind tunnel. The results showed that, under optimal operating conditions, sliding discharge was improved by 3%. Wang studied the three-dimensional effects of plasma actuators with various electrode shapes, including linear, triangular, serpentine and square configurations.[20] Numerical results show the electron temperature and three-dimensional plasma force vectors for four actuator shapes: linear, triangular, serpentine, and square. Subrata introduced

†Corresponding author. E-mail: ymh@xaut.edu.cn

© 2025 Chinese Physical Society and IOP Publishing Ltd. All rights, including for text and data mining, AI training, and similar technologies, are reserved.

a horseshoe actuator configuration, and the numerical results demonstrated that these electrode shapes have a significant three-dimensional effect on the adjacent airflow.[21] Kornilov introduced a distinct approach known as the near-wall micro-blowing technique to enhance TBL coherent structure control.[22] Jin integrated the near-wall micro-blowing method with DBD control to develop a novel actuator called the annular dielectric barrier discharge (A-DBD) plasma actuator,[23] combining the benefits of DBD stabilized discharge and micro-blowing with potent zero-mass blowing and suction control effects. This technique induces localized blowing and suctioning to alter the vortex structure within the TBL. The A-DBD plasma actuator generates a wall-normal jet through interaction with counter-tangential streams, significantly affecting the entire flow field. Its application in TDR greatly enhances control effectiveness compared to previous methods.

However, the influence range of a single annular DBD plasma actuator is limited. Although the array structure is used to expand the range of action, the arrangement of the ring array does not allow interaction between individual actuators and lacks overall control. To this end, this paper proposes a sector-shaped counter-flow DBD (SSC-DBD) plasma actuator, which transforms the original annular electrode into a C-port-shaped electrode and arranges the actuators symmetrically based on jet synthesis. This design aims to expand the influence range of the actuator and enhance its efficiency. According to existing research, oscillatory actuation and pulse actuation can suppress the band structure of turbulent boundary layers. In this study, at an inflow velocity of 9.6 m/s ($Re = 1.445 \times 10^4$), we investigate changes in the boundary layer downstream from the plasma actuator. The focus is on the effects of different actuation frequencies f and voltages V on controlling the turbulent boundary layer over a flat plate, with a brief analysis of the drag reduction mechanism.

2. Experimental system

2.1. Sector-shaped counter-flow DBD plasma actuator

The SSC-DBD plasma actuator consists of a symmetric set of C-shaped exposed electrodes with sector angles of 240° and a ring-shaped buried electrode, separated by a 1 mm PCB board with a dielectric constant of 4.7 (Fig. 1). Both electrodes are made of 0.05 mm thick copper foil. They are aligned along the same axis without any horizontal spacing. Due to the absence of horizontal spacing, plasma discharge from the high-voltage electrode is directed towards the ground electrode, forming a plasma jet through the sectors. The annular exposed electrode has a width of 2 mm and an inner radius of 10 mm, while the covered electrode has a width of 20 mm. To prevent arc discharge between the electrodes, a 0.3 mm thick Kapton insulating tape is applied over the buried electrode for additional insulation.

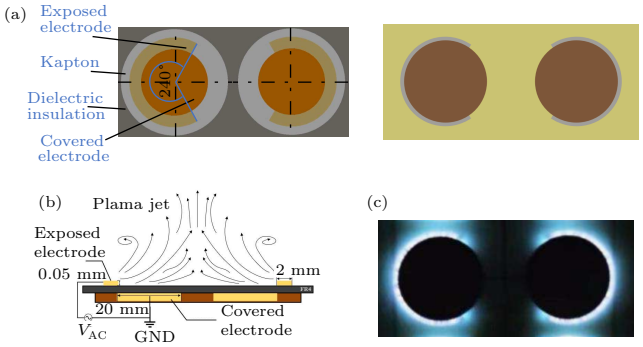


Fig. 1. (a) The structure diagram of an SSC-DBD plasma actuator with a 240° sector angle, (b) electrical connection, (c) plasma discharge region (top view).

A CTP-2000K low-temperature plasma experimental power supply, rated at 500 W, was used, providing sinusoidal output voltages ranging from 0 to 30 kV and frequencies between 5 kHz and 20 kHz. The experiment was conducted in both steady and unsteady modes. A digital pulse modulator generated control signals with varying pulse frequencies and duty cycles. The timing of these control signals was adjusted to create the driving waveform shown in Fig. 2 for pulsed operation. The pulse frequency (f_p) and duty cycle (τ) are defined by

$$f_p = \frac{1}{T}, \tag{1}$$

$$\tau = \frac{T_{on}}{T} \times 100\%. \tag{2}$$

The voltage and current data of the plasma actuator are collected by the Tektronix P6015A and Pearson Model 2877, respectively. These signals are then transmitted through 1 MΩ and 50 Ω coaxial cables to the DPO2024 oscilloscope for display.

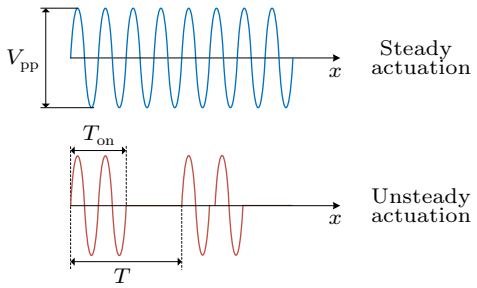


Fig. 2. Pulse modulation waveform diagram.

2.2. Wind tunnel experimental setup

The experiment was conducted in a low-speed wind tunnel at Northwestern Polytechnical University, as illustrated in Fig. 3.[9] The wind speed was adjustable from 0 to 20 m/s, with a fixed incoming velocity of 9.6 m/s ($Re = 1.445 \times 10^4$) and background turbulence below 0.3%. The experimental section measured 670 × 720 × 200 mm and featured a rectangular cross-section with the lower wall machined from a single block of acrylic sheet. A 130 mm × 130 mm square step was

integrated into the lower wall panel to install fixed experimental equipment. The upper wall plate, constructed of rigid steel, housed a rectangular measuring port measuring 670 mm in length along the flow direction and 220 mm in width across the spreading direction. Through this port, the top section of the wind tunnel accommodated a 3D displacement-measuring system with a hot-wire sensor, enabling the collection and analysis of flow-field data.

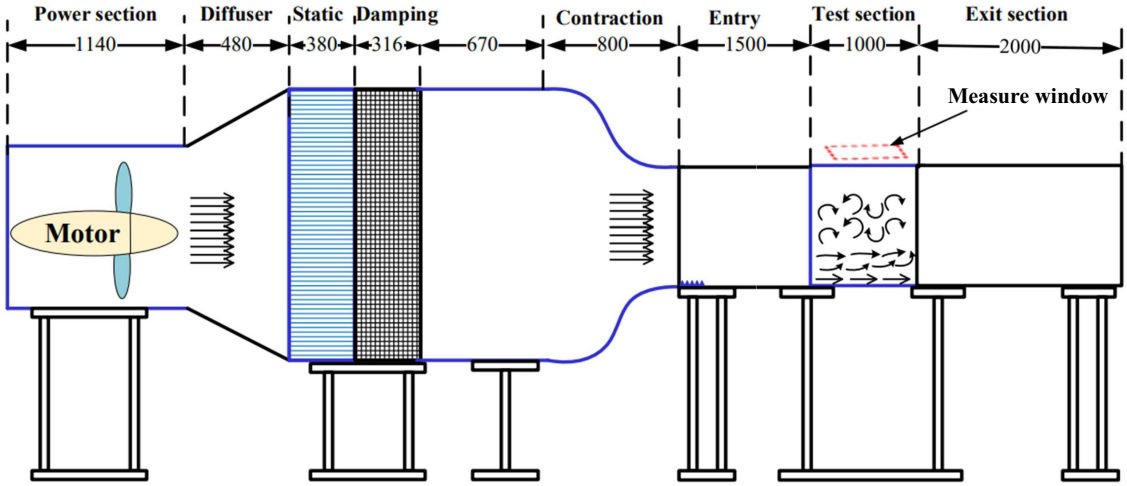


Fig. 3. Schematic diagram of the low-speed wind tunnel.[9]

To ensure the complete development of the TBL within the wind tunnel's test section, a 50 mm wide strip of 120-grit sandpaper was affixed to the wall, 150 mm downstream from the converging section outlet. This strip of surface roughness acts as a transition element to facilitate the full development of the TBL in the experimental section. The flat model was constructed from the same insulated plexiglass sheet as the sidewalls for safety reasons. In the subsequent section, the model was positioned within a square step, and to prevent experimental errors caused by surface irregularities, its upper surface was aligned flush with the lower wall. The schematic diagram of the lower wall panel is shown in Fig. 4.

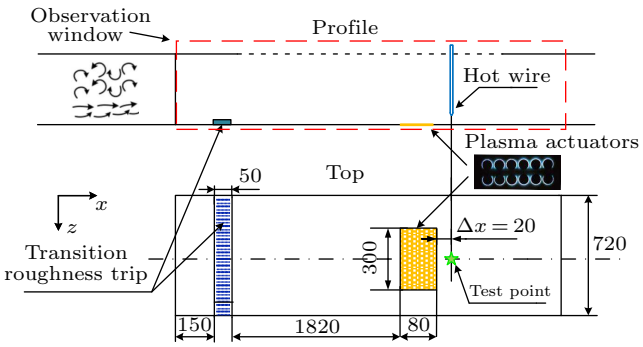


Fig. 4. Schematic diagram of the experimental layout.

For this experiment, a matrix arrangement of 2×6 exposed electrodes was implemented, as illustrated in Fig. 5. The gap between the exposed electrodes is $\Delta d = 3$ mm, and the radius of the covered electrodes is $r = 10$ mm. The distance between the centers of the adjacent actuators is $d = 30$ mm, with a separation of $h = 25$ mm between neighboring actuators. The covered electrodes are embedded in the center of the actuators and protected by a 0.3 mm thick Kapton layer to prevent arcing during discharge.

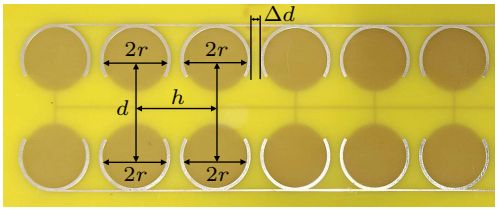


Fig. 5. SSC-DBD plasma actuator array structure.

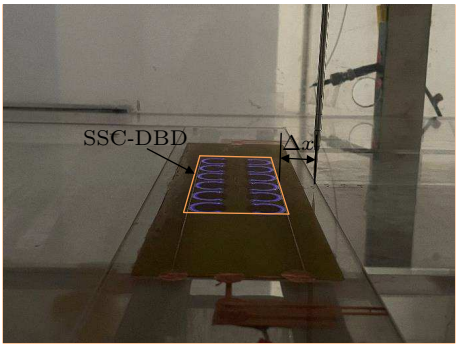


Fig. 6. SSC-DBD actuator installation and plasma discharge experiment diagram.

For acquiring pulse velocity distribution profiles, a hot-wire velocity probe (55P15), coupled with a Dantec StreamLine thermostat, was used for data acquisition. In this experiment, precise probe positioning was crucial for accurate data acquisition. The hot-wire probe was placed at the actuator's central axis, with data collected 20 mm downstream from the actuator for subsequent analysis. The main components of the hot-wire anemometer included a central unit and a calibrator. The 55P15 probe was calibrated for velocity voltage using

an automatic calibration unit designed explicitly for hot-wire anemometers, covering a calibrated velocity range, as shown in Fig. 6.

3. TDR experimental results with sector-shaped counter-flow dielectric barrier discharge

In this experiment, the fixed incoming velocity of the wind tunnel was set at 9.6 m/s ($Re = 1.445 \times 10^4$). The boundary layer thickness (δ) in the uncontrolled state was determined to be 58.50 mm based on the analysis of experimental velocity data. The Clauser (1956) equation was employed in this study to fit the velocity within the logarithmic region of the boundary layer using the least-squares method.[22] The equation is as follows:

$$u^+ = 2.44 \ln y^+ + 4.9. \tag{3}$$

The correlation involving the friction velocity $u_{\tau i}$ and the time-averaged arrangement of (y_i, u_i) obtained from the measurements can be established, where i corresponds to varying normal distances,

$$\frac{y_i u_i}{\nu} = f\left(\frac{u_i}{u_{\tau i}}\right), \tag{4}$$

$$R^2 = 1 - \frac{\sum_i (\hat{y}_i - y_i)^2}{\sum_i (\bar{y}_i - y_i)^2}. \tag{5}$$

From Eq. (4), it is evident that each time-averaged sequence (y_i, u_i) in the logarithmic region corresponds to a friction velocity value $u_{\tau i}$, with $u_{\tau i}$ being the only unknown variable. By performing least-squares fitting on all time-averaged sequences in the logarithmic region, the goodness of fit R^2 approaches 1, and the optimal friction velocity value u_τ is obtained.

The friction coefficient C_f and the wall shear stress $\tau_\mathrm{w} = \rho u_\tau^2$ are obtained by fitting the velocity profile to the Eq. (6) described. The DR rate is used to quantify the amount of drag reduction

$$C_\mathrm{f} = \frac{\tau_\mathrm{w}}{1/2\rho U_\infty^2} = 2\left(\frac{u_\tau}{U_\infty}\right)^2, \tag{6}$$

$$\mathrm{DR} = 1 - \frac{\tau_{\mathrm{w-on}}}{\tau_{\mathrm{w-off}}} 100\%. \tag{7}$$

In the above equation, DR represents the drag reduction rate. When DR > 0 indicates that the system's actuation reduces drag; DR < 0 indicates that the plasma actuation increases drag. $\tau_{\mathrm{w-off}}$ represents the wall shear stress at the measurement point when the plasma actuator is turned off, while $\tau_{\mathrm{w-on}}$ represents the wall shear stress when the actuator is turned on.

Figure 7 illustrates the boundary layer velocity distribution with the device turned off. The figure reveals that the velocity distribution within the logarithmic region ($50 < y^+ < 200$), measured 20 mm downstream from the actuator, closely follows the classical logarithmic law (Clauser's equation). This suggests that the boundary layer in the measurement region has adequately developed into the TBL. Consequently, this indicates that the actuator is correctly positioned, its influence range precisely matches the TBL, and its placement does not hinder the normal development of the boundary layer.

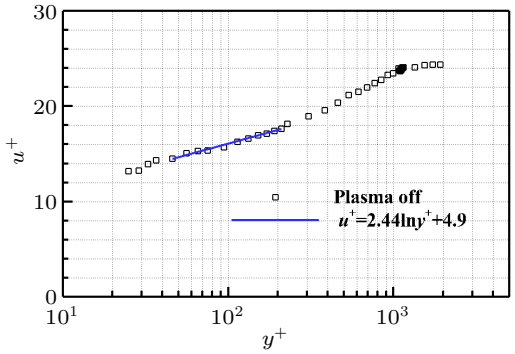


Fig. 7. Influence of SSC-DBD plasma actuator arrangement on TBL.

3.1. TDR experimental results with plasma actuation

3.1.1. Turbulent drag reduction control effect at different pulse frequencies

When investigating TDR at various pulse frequencies, all other parameters were kept constant, with the actuation voltage fixed at 9 kV. Velocity distributions at different frequencies were standardized using the corresponding internal scales of the boundary layer u_τ, resulting in overlapping velocity distributions. This consistency arises from the use of specific internal scales for dimensionless scaling.

Previous research has identified a coupling frequency where matching the pulse frequency of the plasma driver with the intrinsic frequency of the incoming flow enhances flow control effectiveness, similar to resonance.[24] To leverage this phenomenon for optimizing flow control parameters and effectiveness, we examined the impact of actuation on turbulent friction resistance across different pulse frequencies. The incident flow velocity was kept constant at 9.6 m/s ($Re = 1.445 \times 10^4$), with the actuation voltage set at 9 kV and a duty cycle τ of 50%. This analysis builds upon prior experimental investigations involving various pulse frequencies ($f_\mathrm{p} = 50$ Hz, 100 Hz, 200 Hz, 400 Hz and 800 Hz), demonstrating varying degrees of effectiveness in reducing frictional resistance.

However, when different pulse frequencies are applied, changes in the velocity distribution within the boundary layer become evident. Notably, a significant decrease in velocity is observed in both the buffer layer and the logarithmic region. After actuation, the jet interacts with the flow near the wall. The actuator-induced reverse vortex creates a "virtual barrier"

effect near the wall, lifting away downstream vortices and coherent structures adjacent to the wall. As a result, frictional drag from interactions between downstream vortex sweeping events is mitigated. Simultaneously, the regeneration of downstream vortices near the wall is hindered, leading to reduced velocities in the buffer layer and logarithmic region. Ultimately, this contributes to achieving TDR.

Figure 9 compares the velocity distributions across various boundary layers at different pulse frequencies, alongside that of an uncontrolled boundary layer. Here, u^+ represents the dimensionless flow velocity and y^+ denotes the dimensionless wall distance,

$$y^+ = \frac{y}{\delta_v} = \frac{yu_\tau}{\nu}, \tag{8}$$

$$u^+ = \frac{u}{u_\tau}, \tag{9}$$

where ν represents the kinematic viscosity of air and u_τ is the wall friction velocity. These velocity distributions were processed dimensionless using the internal scale of the uncontrolled boundary layer. The phenomenon observed in Fig. 9 illustrates changes in velocity distributions after applying various pulse frequencies. This change is characterized by a velocity deficit, indicated by a downward shift in velocity profiles within the logarithmic zone compared to the uncontrolled boundary layer. Notably, lines representing different pulse frequencies show significant downward shifts to varying degrees, indicating different levels of streamwise velocity reduction within the boundary layer across various pulse frequencies. However, the velocity distribution of the boundary layer changes after applying different pulse frequencies, and the velocities of the buffer layer and the logarithmic region decrease significantly. Figure 8 presents a schematic diagram of the classical wall turbulence layered model. The blue line represents the logarithmic distribution predicted by Clauser's classical theory, while the black points indicate the time-averaged velocity measured at the specified points when the actuator is off. The close agreement between the two confirms the validity of the model. In contrast, the colored points depict the time-averaged velocity measured after the actuator is activated, with the degree of offset indicating the drag reduction effect. Compared to the velocity profile without actuation, an upward displacement of the velocity curve corresponds to an increase in friction velocity, indicating higher surface friction resistance and increased drag. Conversely, a downward displacement corresponds to a decrease in friction velocity, reflecting reduced surface friction resistance and drag. The relationship is described by

$$\tau_{\omega i} = \rho u_{\tau i}^2. \tag{10}$$

A greater degree of offset signifies a more effective drag reduction.

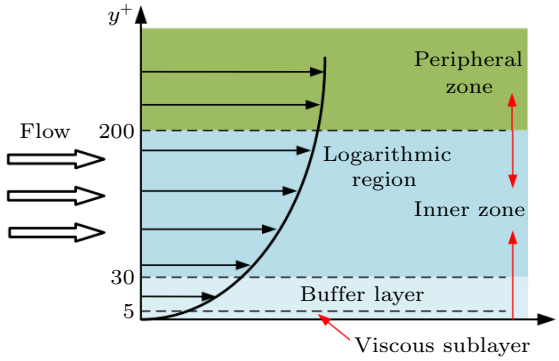


Fig. 8. Schematic diagram of the classical wall turbulent layered model.

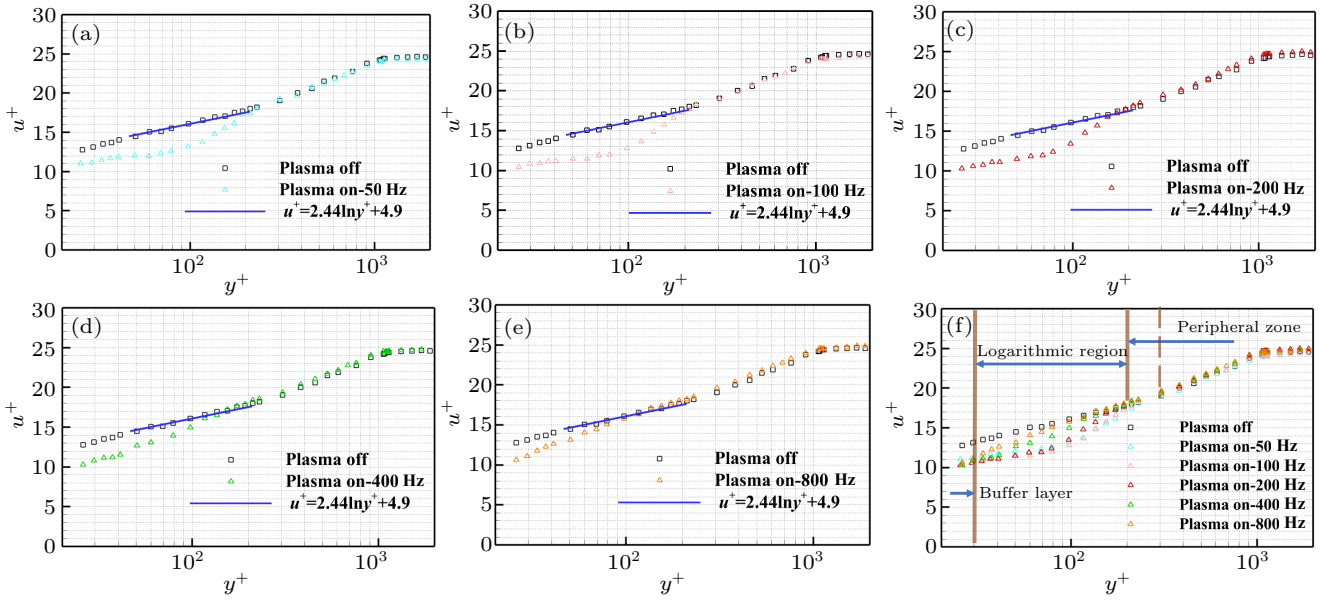


Fig. 9. Comparing boundary layer velocity distributions across various pulse frequencies. (a) $f_p = 50$ Hz, (b) $f_p = 100$ Hz, (c) $f_p = 200$ Hz, (d) $f_p = 400$ Hz, (e) $f_p = 800$ Hz, (f) velocity distributions across various pulse frequencies.

Furthermore, beyond $y^+ > 200$, the boundary layer velocity distribution closely resembles that of the uncontrolled boundary layer, highlighting the localized impact of plasma aerodynamic actuation within a specific operational range, particularly in the logarithmic region of the TBL and its adjacent areas. In addition, increasing pulse frequency correlates with an initial increase followed by a tapering of velocity reduction within the $300 < y^+ < 1000$ range. Across different frequencies, the velocity distributions show substantial overlap, indicating consistent patterns across all five frequencies. These findings suggest that the limited operational scope of plasma actuation may be due to this observed trend.

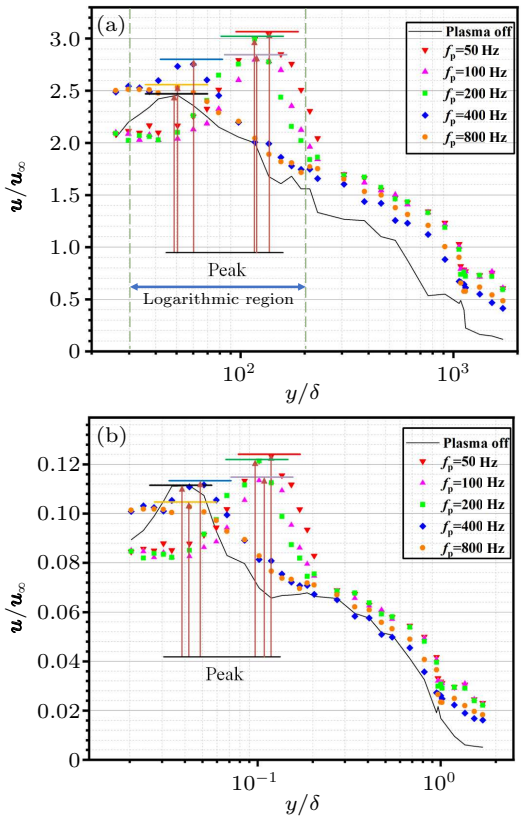


Fig. 10. Dimensionless velocity fluctuation distributions under various pulse frequencies: (a) inside the TBL, (b) outside the TBL.

Velocity fluctuation distributions inside and outside the TBL were analyzed using dimensionless methods. Figure 10 present comparative results of these distributions across various pulse frequencies. Both actuated and un-actuated scenarios adhere to classical TBL theory, where root mean square velocities initially increase and decrease.[25] However, variations in peak values are evident. Specifically, at a frequency of 50 Hz, post-actuation, longitudinal vortex positions rise, promoting their migration to higher regions. The peak at 50 Hz (the line in the peak) is the highest among the groups used. This fosters fluid mixing between low-velocity and high-velocity zones, leading to deviations in peak velocity fluctuation distributions and contributing to drag reduction. Remarkably, 50 Hz demonstrates the most effective drag reduction among the tested frequencies. None of the pulse frequencies yield velocity fluctuation distributions with peaks lower than the baseline, indicating increased frictional resistance. Nevertheless, these differences in drag reduction effectiveness do not result in drag increase phenomena across the tested frequencies. Analysis suggests that when the applied pulse frequency exceeds optimal control parameters, the generation of jet-induced coherent structures becomes more frequent. This intensifies velocity fluctuations within the buffer and logarithmic zones, reducing drag reduction efficiency or potentially causing drag increase phenomena.

Table 1 shows the variation of the boundary layer correlation parameters at different pulse frequencies. Combined with Fig. 11, it illustrates the variations in resistance reduction rate and friction coefficient across different pulse frequencies. The most significant localized reduction in resistance, reaching 20.97%, occurs when the incoming flow velocity is 9.6 m/s ($Re = 1.445 \times 10^4$), the actuation voltage is 9 kV and the pulse frequency is 50 Hz. However, as the pulse frequency increases, the reduction in resistance gradually diminishes. For instance, at a pulse frequency of 800 Hz, the applied actuation results in only a 3.4% drag reduction.

Table 1. Parameter comparison of boundary layer with different pulse frequencies.

f (Hz)	u_τ (m/s)	τ_w (Pa)	C_f	DR
Off	0.2838	0.09544	0.00331	–
50	0.2523	0.07543	0.00261	20.97%
100	0.2607	0.08054	0.00279	15.61%
200	0.2719	0.08761	0.00304	8.2%
400	0.2749	0.08955	0.00310	6.17%
800	0.2790	0.09224	0.00320	3.35%

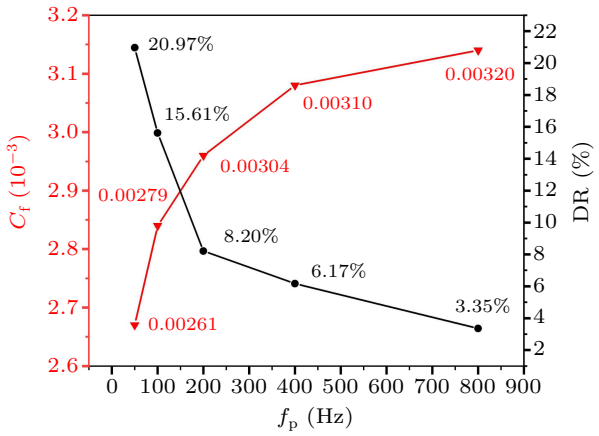


Fig. 11. The drag coefficient and drag reduction ratio under various pulse frequencies.

A corresponding matching frequency is essential to achieve optimal control efficacy. If the pulse frequency exceeds the incoming flow frequency, it amplifies the energy and spatial scale of actuation-induced flow structures beyond what is necessary for the incoming flow. This discrepancy might induce the formation of secondary longitudinal vortices, inten-

sify longitudinal vortices near the wall, and consequently reduce the thickness of the viscous sublayer. As a result, control effectiveness may decrease or even lead to complete failure.

3.1.2. Turbulent drag reduction control effect at different actuation voltages

This section investigates how different actuation strengths affect turbulent frictional resistance while maintaining a constant incoming velocity of 9.6 m/s ($Re = 1.445 \times 10^4$) and a carrier frequency of 10 kHz. The primary objective is to examine the variations in TBL frictional resistance under different actuation voltages.

Figure 12 depicts the comparison of velocity distributions within the boundary layer under various applied actuation voltages, normalized using the internal scale of the boundary layer without actuation. Significant changes in the velocity distributions within the boundary layer are discernible after applying different actuation voltages, particularly in the buffer layer and logarithmic region. A decrease in controlled velocity compared to the baseline flow velocity signifies a reduced wall friction velocity under controlled circumstances. This reduction in controlled velocity correlates with a decrease in surface frictional resistance, where a larger deviation indicates a more pronounced decrease in resistance.

In the region where $y^+ < 80$, the actuation application leads to varying degrees of downward deviation in velocity distribution. However, in the $80 < y^+ < 175$ range, increasing actuation voltage gradually reduces the velocity deviation within the buffer layer and logarithmic zone, thereby diminishing control effectiveness. This indicates that, for a given incoming flow rate, stronger actuation does not necessarily yield better outcomes.[26,27] Instead, an optimal actuation strength exists, maximizing drag reduction, similar to findings in prior studies on drag reduction in flat-plate boundary layers.[28] Beyond $y^+ > 175$, the effectiveness of the actuator diminishes, with velocity distributions within the boundary layer controlled and uncontrolled, mainly overlapping. This suggests that the current actuator configuration and parameters primarily influence near-wall longitudinal vortex structures within the buffer layer, viscous sublayer and logarithmic region.

In previous experiments, when the input energy matched the strength of the flow field, the jet interacted with the near-wall flow, facilitating mass and momentum transport, and influencing the boundary layer flow. This process inhibited the regeneration of longitudinal vortex structures, leading to a velocity deficit in the buffer layer and logarithmic region, ultimately achieving the goal of TDR. However, if the applied intensity exceeds a certain threshold, it amplifies the intensity of longitudinal vortices in the near-wall region, resulting in increased wall friction resistance. Nonetheless, in this scenario, the selected actuation voltage does not exceed this threshold, as depicted in Fig. 12. There is no noticeable upward shift in the plot line after actuation, nor any indication of increased drag.

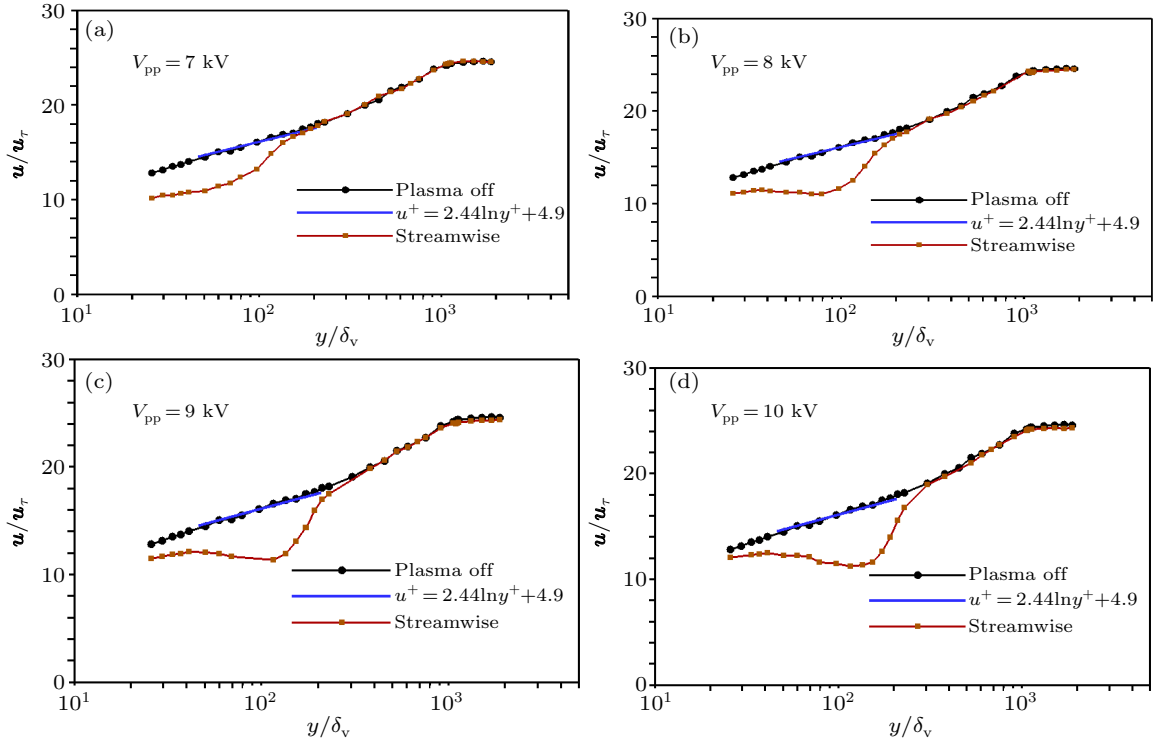


Fig. 12. Comparing boundary layer velocity distributions at various actuation voltages.

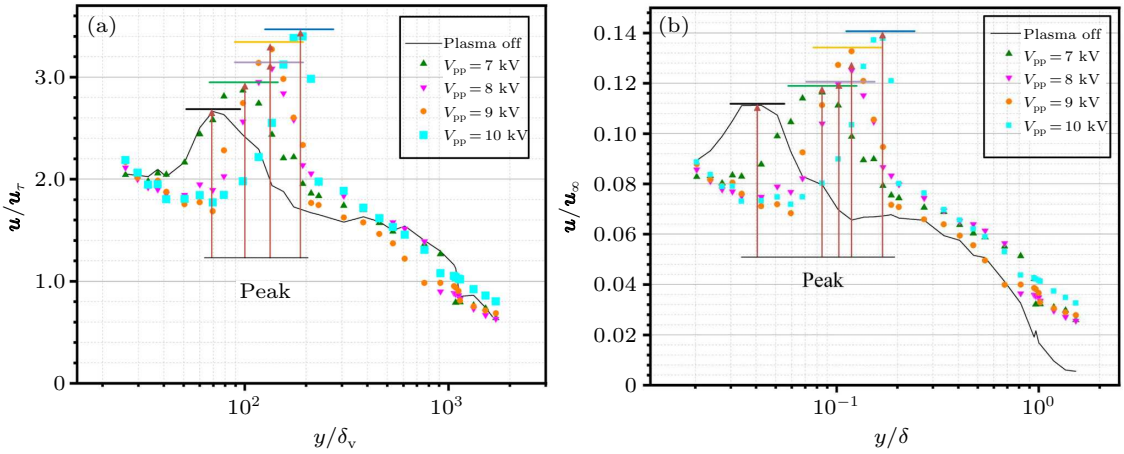


Fig. 13. Flow direction velocity fluctuation distributions at various actuation voltages.

Figure 13 depict the comparative results of velocity fluctuation distributions under different actuation voltages. Specifically, figure 13 illustrates the boundary layer's dimensionless inner and outer scales without actuation. In this state, the root mean square velocity demonstrates the classical pattern of increasing and then decreasing with height, consistent with TBL theory. Notably, figure 13 shows that the peak-controlled pulsation velocity increases with higher actuation voltage and blowing intensity. This increase corresponds to an upward shift in the spatial location of the longitudinal vortex structure, which progressively moves upwards as actuation voltage and blowing intensity increase.

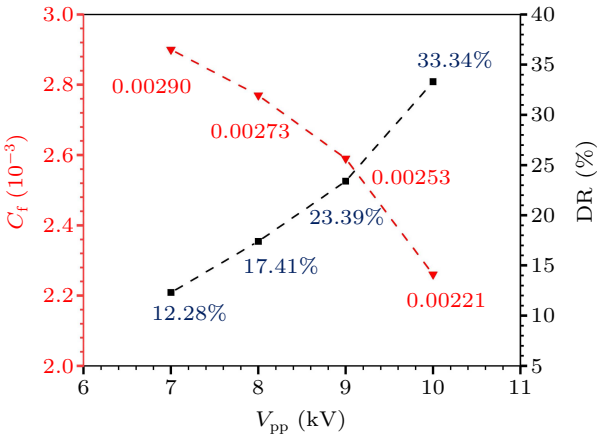


Fig. 14. Comparing boundary layer velocity distributions across various actuation voltages.

Table 2 shows the variation in the boundary layer's correlation parameters at different actuation voltages. The subsequent analysis systematically estimates the surface friction coefficient and drag reduction rate using the viscous sublayer law fitting established earlier. Figure 14 illustrates the variations in drag reduction rate and friction coefficient under different actuation voltages. Notably, an optimal localized drag reduction of 33.34% is achieved at an actuation voltage of $V_{pp} = 10$ kV. Significantly, no trend of the friction coefficient gradually increasing or the drag reduction effect gradually decreasing is observed with increasing actuation voltage. This absence of such a phenomenon suggests that the selected voltage parameter has not yet reached its threshold. Consequently, the figure shows a continuous increase in drag reduction rate with the rise in actuation voltage.

Table 2. Parameter comparison of boundary layer with different actuation voltages.

V (kV)	u_τ (m/s)	τ_w (Pa)	C_f	DR
Off	0.2838	0.09544	0.00331	–
7	0.2658	0.08372	0.00290	12.28%
8	0.2579	0.07882	0.00273	17.41%
9	0.2484	0.07312	0.00253	23.39%
10	0.2317	0.06362	0.00221	33.34%

3.2. Analysis of resistance reduction mechanism

The upward jet flow removes the low-speed streaks near the wall, leading to a reduction in speed in this region compared to the uncontrolled boundary layer, thereby inducing a drag reduction effect. The jet interacts with the turbulent near-wall flow, and the induced jet works to disrupt the self-sustaining streamwise vortices in the turbulent boundary layer by interrupting the sweep events of these vortices, as illustrated in Fig. 15.

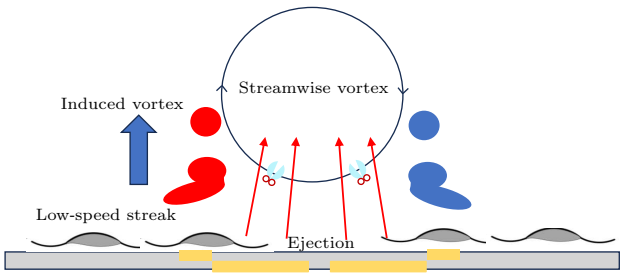


Fig. 15. Schematic diagram of the blowing TDR strategy.

When the SSC-DBD is activated, it generates vortices perpendicular to the wall, which evolve into large-scale streamwise vortices (LSSVs) in the near-wall region of the boundary layer. These vortices suppress wall interactions by

inhibiting the development of streamwise vortices and streak structures near the wall. The perpendicular vortices restrain the spanwise movement of the streaks, stabilizing them and creating a riblet-like effect. This virtual riblet effect reduces drag and lowers turbulence intensity, with the drag reduction increasing as the virtual riblet effect becomes more dominant, ultimately achieving the goal of turbulent drag reduction.

4. Conclusion

In summary, the experiment evaluates the actuator's drag reduction effectiveness under different environmental conditions by adjusting various parameters. The wall friction velocity U_τ is determined through logarithmic zone velocity fitting and velocity data are normalized. Based on a comprehensive analysis of boundary layer velocity distribution, the following conclusions are drawn.

(i) The drag reduction effect is most effective when there is a coupling relationship between the plasma pulse frequency and the natural frequency of the external flow field. Various pulse frequencies of plasma aerodynamic actuation were employed to achieve localized drag reduction control, and the drag reduction rate gradually decreased as the actuation frequency increased. The maximum local drag reduction rate reached approximately 20.97% at $f_\mathrm{p} = 50$ Hz. Compared with previous studies,[22] the effect increased by 1.23 times.

(ii) When the inflow velocity is constant, the actuation intensity needs to match the inflow intensity. In this experiment, with an inflow velocity of $U_\infty = 9.6$ m/s ($Re = 1.445 \times 10^4$), the friction coefficient gradually decreases as the actuation voltage increases, and the drag reduction effect gradually improves. Based on this analysis, an optimal actuation voltage of $V_\mathrm{pp} = 10$ kV is identified, resulting in a maximum drag reduction effect of 33.34%. We compared our results with the ring actuator under a 7 m/s incoming flow, which showed a drag reduction of 17.72% at a V_pp of 8 kV. Our results demonstrated a drag reduction effect 1.88 times greater.

(iii) Under the drag reduction conditions of this experiment, the logarithmic velocity distribution of the turbulent boundary layer exhibited a significant downward shift, with the logarithmic velocity decreasing notably.

This paper investigates the application of the SSC-DBD plasma actuator for reducing drag in the turbulent boundary layer (TBL). This innovative approach enhances plasma control over incoming flow velocity, representing a significant advancement in TBL drag reduction compared to previous methods. Future research will incorporate high-speed particle image velocimetry (PIV) to visualize flow changes and monitor alterations in coherent structures within the TBL induced by plasma pneumatic actuation. This comprehensive study aims to elucidate the underlying mechanisms of the plasma actuator, focusing on vortex development processes and their implications for drag reduction efficiency. Ultimately, this research will enable more precise and effective drag reduction control. The development of induced vortices on both sides has not been fully explored, and the drag reduction parameters in this study should be validated in future research to examine the differences and evolution of the induced vortices.

Acknowledgment

Project supported by the National Natural Science Foundation of China (Grant Nos. 61971345 and 52107174).

References

[1] Bushnell D M 2003 *Journal of Aerospace Engineering* **217** 1
[2] Abbas A, Bugeda G and Ferrer E 2017 *Science China Technological Sciences* **60** 1281
[3] Marusic I, McKeon B J, Monkewitz P A, *et al.* 2010 *Phys. Fluids* **22** 065103
[4] Corke T C and Thomas F O 2018 *AIAA Journal* **56** 3835
[5] Perlin M and David R 2016 *Journal of Fluids Engineering* **138** 9
[6] Zhao Z, Jiang R and Feng J 2022 *Ocean Engineering* **253** 111266
[7] Wang J J, Li Y C and Choi K S 2008 *Progress in Aerospace sciences* **44** 22
[8] Nesselrooij M V, Veldhuis L, Oudheusden B V and Schrijer F 2016 *Exp. Fluids* **57** 142
[9] Lu L S, Li D and Zheng J 2020 *Advances in Aeronautical Science and Engineering* **11** 5
[10] Yao J, Chen X and Thomas F 2017 *Phys. Rev. Fluids* **2** 062601
[11] Yao J, Chen X and Hussain F 2018 *J. Fluid Mech.* **852** 678
[12] Zheng B R, Ke X and Ge C 2020 *AIAA Journal* **58** 1
[13] Lei Y, Dong S, Liang R, Feng Y, Xiang S and Chen K 2024 *IEEE Transactions on Plasma Science* **52** 867
[14] Yang L L, Cai J S and Kang L 2017 *High Voltage Engineering* **43** 6
[15] Zhao L S, Dong S L, Xiang S Z, Mao S P, Lei Y, Zhang P H, Yu L and Yao C G 2024 *IEEE Transactions on Industrial Electronics* **71** 12086
[16] Shang J S and Huang P G 2014 *Progress in Aerospace Sciences* **67** 29
[17] Jukes T, Choi K S and Johnson G A 2006 *AIAA Flow Control Conference* **14** 3693
[18] Whalley R and Choi K S 2011 *Journal of Physics* **318** 022039
[19] Whalley R and Choi K 2011 *5th Flow Control Conference*
[20] Wang C C and Ryan D 2011 *J. Appl. Phys.* **109** 083305
[21] Roy S and Wang C C 2009 *J. Phys. D: Appl. Phys.* **42** 032004
[22] Kornilov V 2015 *Progress in Aerospace Sciences* **76** 1
[23] Zheng B R, Jin Y and Yu M H 2022 *Plasma Science and Technology* **24** 114003
[24] Zheng B R, Xue M and Ge C 2020 *Chin. Phys. B* **29** 064703
[25] Pope S B 2001 *Measurement Science and Technology* **12** 11
[26] Cheng X Q, Qiao Z X and Zhang X 2021 *J. Fluid Mech.* **920** A50
[27] Wu B, Gao C and Liu F 2019 *Plasma Science and Technology* **21** 045501
[28] Thomas F O, Corke T C and Duong A 2019 *J. Phys. D: Appl. Phys.* **52** 434001
[29] Ran W, Zare A and Jovanović M R 2021 *J. Fluid Mech.* **906** A7